MR imaging of apparent ^{3}He gas transport in narrow pipes and rodent airways

Kevin R. Minard [a,*], Richard E. Jacob [a], Gernot Laicher [b], Daniel R. Einstein [a], Andrew P. Kuprat [a], Richard A. Corley [a]

[a] Pacific Northwest National Laboratory, P.O. Box 999, MSIN P7-58, Richland, WA 99352, USA
[b] University of Utah, Salt Lake City, UT 84112, USA

ABSTRACT

High sensitivity makes hyperpolarized ^{3}He an attractive signal source for visualizing gas flow with magnetic resonance (MR) imaging. Its rapid Brownian motion, however, can blur observed flow lamina and alter measured diffusion rates when excited nuclei traverse shear-induced velocity gradients during data acquisition. Here, both effects are described analytically, and predicted values for measured transport during laminar flow through a straight, 3.2-mm diameter pipe are validated using two-dimensional (2D) constant-time images of different binary gas mixtures. Results show explicitly how measured transport in narrow conduits is characterized by *apparent* values that depend on underlying gas dynamics and imaging time. In ventilated rats, this is found to obscure acquired airflow images. Nevertheless, flow splitting at airway branches is still evident and use of 3D vector flow mapping is shown to reveal surprising detail that highlights the correlation between gas dynamics and lung structure.

© 2008 Published by Elsevier Inc.

1. Introduction

Magnetic resonance (MR) imaging with hyperpolarized xenon (^{129}Xe) or helium (^{3}He) affords high sensitivity for measuring gas flow in straight pipes [1,2], porous foam [3], flexible tubes [4], human airway models [2,5], and breathing patients [2]. Flow quantification, however, is challenged by rapid gas diffusion. This is especially problematic in small conduits where diffusing gas can readily sample shear-induced velocity gradients over the imaging time (t). In phase-contrast MR images this has been observed to blur laminar flow in small capillaries [1]. For a pipe of radius a, and gas molecules with diffusion coefficient D, results show that the degree of blurring can be significant—even over relatively short time scales ($t < a^2/D$). Since axial diffusion is also found to be time-dependent [1], prior work suggests that MR measurements of gas transport in narrow conduits provide apparent values that depend on underlying flow structure, gas diffusion, and imaging time.

Recent work on gas-phase MR stresses its potential utility for visualizing gas dynamics in applications ranging from toxicology [6] and inhaled drug delivery [2] to catalytic [7] and aeronautic design [8]. In related studies, most results have been acquired in larger conduits where the imaging time (t) is short relative to gas diffusion and flow structure. Blurring effects have therefore been ignored, and to a large extent, good agreement between measured flow and predictions based on computational fluid dynamics (CFD) has been observed [2,5,8]. Even in these studies, however, subtle

differences are apparent in regions where strong velocity gradients exist on diffusive length scales. In small capillaries, Monte Carlo simulations suggest that these differences might be attributable to diffusion-mediated sampling of multiple flow streams during image collection [1]. Nevertheless, no analytical description of this phenomenon has yet been formulated. Furthermore, no measurements of ^{3}He flow in narrow conduits of complex shape have yet been reported. It is therefore unclear what information might be available, or to what extent it might be limited by diffusion-mediated effects.

Prior work on gas transport in small capillaries employed one-dimensional (1D) flow imaging, axial diffusion was not resolved, and results were understood through Monte Carlo simulations [1]. Here, imaging is extended to two- and three-dimensions to facilitate transport measurements in more complex systems, and apparent gas dynamics in straight pipes is described analytically to provide deeper physical insight. Analytical theory explicitly accounts for gas dynamics, incorporates the details of MR data acquisition, and is shown to accurately predict the combined effects of flow and diffusion over a range of experimental conditions. In live rats, these effects are found to obscure laminar flow in pulmonary airways, thereby, confounding any direct comparison with CFD predictions. Despite this limitation, however, 3D images of in vivo airflow are shown to provide a detailed view of pulmonary airflow patterns not yet seen. Hallmarks include the visualization of flow streaming similar to that recently reported in humans [2], and detailed flow splitting at airway branches that may provide a quantitative basis for assessing ventilation to each of the rat's five lung lobes.

* Corresponding author. Fax: +1 509 376 2303.
E-mail address: kevin.minard@pnl.gov (K.R. Minard).

2. Theory

2.1. Structure and function of constant-time imaging (CTI)

During MR imaging random Brownian motion causes irreversible signal loss that reduces sensitivity and fundamentally limits resolution [9–11]. Constant-time imaging (CTI) minimizes both adverse effects [12,13], and for this reason, is increasingly used for gas visualization [6,8,14,15]. Its simple structure and function is also easily understood, and here, this facilitates a rigorous description of measured gas transport.

During a 2D CTI experiment like that shown in Fig. 1, spatial information within the excited slice is phase-encoded along each planar axis. Repeated application of the pulse sequence using different phase encoding gradients is then utilized to collect a motion-sensitive image. Subsequent analysis of images acquired using different motion-sensitizing gradients then provides a basis for local transport measurements [16–18].

As with all MR imaging methods, a finite time is typically required to encode location and motion. In the context of Fig. 1, this means that excited gas molecules can diffuse across shear-induced velocity gradients after their location is initially encoded, and motion-sensitizing gradients are applied. Direct correspondence between location and dynamics is therefore compromised, and this necessarily blurs measured transport. The following theory describes this loss of correspondence and its ensuing affects on measured transport in constant-time images.

2.2. Effects of gas motion on 2D CTI

In this study the slice-select gradient in Fig. 1 is aligned with the central axis of a straight, circular pipe, and 2D phase encoding is employed for visualizing ^{3}He gas over its cross section. Axial flow and diffusion is then measured using the spatially resolved MR signal (S) from two different images—one acquired with motion sensitizing gradients applied along the slice-select axis (S_G), and the other without (S_0).

During data acquisition molecular motion through applied gradients alters the relative phase ϕ and attenuation β of the spatially resolved MR signal at each location r_0 in a motion-sensitized image [16–18]. If 2D phase encoding pulses are short, and gas location is assumed to be instantaneously encoded at $t = 0$ defined in Fig. 1,
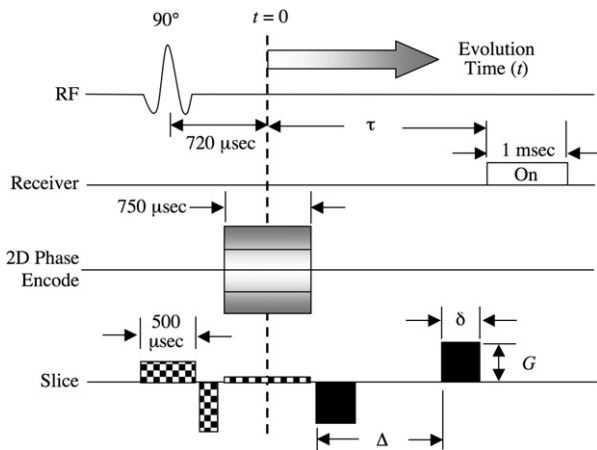

Fig. 1. Timing diagram for 2D CTI. Since slice-select gradients (checkered) are velocity compensated, moving gas is refocused before motion-sensitizing gradients (solid-black) are applied to measure gas dynamics along the same axis. Motion sensitization, however, occurs after a 2D phase encoding gradient (shaded) is applied to resolve planar location at $t = 0$. Consequently, if gas molecules traverse multiple flow streams during the evolution time (t), direct correspondence is lost between planar location and measured transport.

then relative signal changes can be conveniently expressed as an ensemble average ($\langle \rangle$) over all molecules initially encoded at r_0, such that [16,19]—

$$\frac{S_G}{S_0} = e^{i\phi - \beta} = \left\langle e^{i\gamma \int_0^\tau F(t)v(t)\,dt} \right\rangle. \tag{1}$$

Here, γ denotes the gyromagnetic ratio, and $v(t)$ represents each molecule's instantaneous axial velocity. Other parameters include the time (τ) when the NMR receiver is turned on, and the time-integral of motion-sensitizing gradients—

$$F(t) = \int_0^t G(t')\,dt', \tag{2}$$

where $G(t)$ is their time-dependent amplitude, and $F(\tau)$ is taken to be zero at the start of data acquisition [16,20,21].

Since a large number of molecules normally contribute to the spatially resolved MR signal it is useful to relate relative changes to their underlying statistical dynamics [16,19]. In practice, this is facilitated by exploiting Kubo's generalized cumulant expansion theorem, such that [20,21]—

$$i\phi - \beta = \lambda = \sum_{n=1}^\infty (i\gamma)^n \int_0^\tau dt_1 \int_0^{t_1} dt_2 \cdots \int_0^{t_{n-1}} dt_n \langle v(t_1)v(t_2) \cdots v(t_n)\rangle_c F(t_1)F(t_2)\cdots F(t_n). \tag{3}$$

In this expression angular brackets $\langle \rangle_c$ denote cumulant averages over the enclosed quantity. Generally, these completely define underlying statistics, are calculated in terms of ensemble averages ($\langle \rangle$), and are sometimes referred to as connected averages since they vanish if any component (i.e. velocity at different times) is uncorrelated with the others [22,23]. For convenience, the first three cumulants are defined below, and expressions for higher orders are found elsewhere [22,23]—

$$\langle v(t_1)\rangle_c = \langle v(t_1)\rangle, \tag{4}$$

$$\langle v(t_1)v(t_2)\rangle_c = \langle v(t_1)v(t_2)\rangle - \langle v(t_1)\rangle\langle v(t_2)\rangle, \tag{5}$$

$$\langle v(t_1)v(t_2)v(t_3)\rangle_c = \langle v(t_1)v(t_2)v(t_3)\rangle - \langle v(t_1)\rangle\langle v(t_2)\rangle\langle v(t_3)\rangle - \langle v(t_2)\rangle\langle v(t_1)v(t_3)\rangle - \langle v(t_3)\rangle\langle v(t_1)v(t_2)\rangle + 2\langle v(t_1)\rangle\langle v(t_2)\rangle\langle v(t_3)\rangle. \tag{6}$$

Eq. (3) shows that relative phase (ϕ) is determined by the imaginary part of the cumulant expansion (Im λ), that relative attenuation (β) is determined by the real part ($-$Re λ), and emphasizes how both are influenced by motion sensitizing gradients and the statistical dynamics of gas motion along their applied direction. In practice, this general description serves as a convenient theoretical construct that has previously been employed for other MR transport studies [20,21]. Here, integrals are explicitly time-ordered such that $\tau > t_1 > t_2 > \cdots t_n$ [22–24]. Generally, this facilitates the analysis of time-dependent processes [24]. Utilization in the current study, however, is only valid for stationary transport processes since MR images are acquired over time using repeated data acquisitions. Physically, this means that underlying dynamics can only depend on the time intervals between successive observations—rather than the exact time each occurs [25]. Use of Eq. (3) also assumes that relative changes in either image phase or attenuation are dominated by molecular displacements during motion sensitizing gradient pulses, and that the effects of motion during spatial encoding are relatively small. To insure this as much as possible, slice-select gradients in Fig. 1 are velocity compensated, and phase encoding is kept as short as possible [26].

2.3. The statistical dynamics of laminar pipe flow

During constant laminar flow in a straight, circular pipe, moving material is directed down its central axis with a speed (V) that varies with radial distance (r), such that [27,28]—

$$V(r) = V_{\max}(1 - r^2/a^2). \tag{7}$$

Here, a represents the pipe's radius and $V_{\max}$ is twice the average flow speed across the pipe [28].

Generally, Eq. (7) represents a specific solution to the Navier–Stokes equation that is valid when the Reynolds number is less than ~2100, gas density is constant, flow is steady, Newton's law of viscosity applies, and effects near the pipe's entrance and exit are neglected [28]. In the current context, $V(r_0)$ describes the average axial velocity ($\langle v(t = 0) \rangle$) when gas is initially encoded at some radius r_0. At later times, $\langle v(t) \rangle$ changes as encoded gas diffuses down the pipe and across streamlines. To formulate a statistical description of this time-dependent motion it is helpful to think of Eq. (7) as a stationary flow field that is sampled by randomly diffusing gas molecules. If $r(t)$ is a stationary Markov process describing each molecule's random position in the absence of flow [25], $v(t)$ may be thought of as having two distinct contributions. One arises from the flow field itself and is represented using the random function $V(r(t))$. The other describes each molecule's random axial velocity as it diffuses down the pipe in the absence of flow. If this is represented by $u(t)$, then net axial motion is expressed as a simple superposition—

$$v(t) = u(t) + V(r(t)). \tag{8}$$

In the absence of flow (i.e. when $V = 0$), Eq. (8) shows that axial motion is governed by the random velocity fluctuations $u(t)$ that diffusing gas normally exhibits. During flow, diffusion mediated changes in location r determine the precise flow rate a diffusing gas molecule must experience. When diffusion is slow relative to flow structure and imaging time, $V(r(t)) \sim V(r_0)$, and Eq. (8) represents the traditional description of constant flow and diffusion that is widely used for liquid-state studies [16–19]. Here, a more general formulation is proposed by accounting for changes in flow velocity that occur as gas diffuses across streamlines on the imaging time scale. Generally, since a finite time is required to diffuse from one location r to the next, changes in flow velocity are mediated by the dynamics of Brownian displacements and do not occur instantaneously. Rather, causality is insured by an accurate description of gas diffusion and the likelihood that changes in location can occur over any given timescale.

Implicit in Eq. (8) is the assumption that axial velocity fluctuations from molecular diffusion down the pipe (u) are statistically independent of the axial flow (V). Physically, this is not unreasonable since the correlation time for $u(t)$ is much shorter than time needed to diffuse across streamlines. One practical consequence of this is that cumulants for statistically independent processes are additive [22]. As a result,

$$\langle v(t_1)v(t_2) \cdots v(t_n) \rangle_c = \langle u(t_1)u(t_2) \cdots u(t_n) \rangle_c \\ + \langle V(r(t_1))V(r(t_2)) \cdots V(r(t_n)) \rangle_c, \tag{9}$$

and effects from axial diffusion (u) and flow (V) can be treated separately, such that—

$$\lambda = \lambda_u + \lambda_V. \tag{10}$$

Since $u(t)$ describes axial velocity fluctuations for diffusing gas in the absence of flow, and these are completely random on the imaging time scale, their average ($\langle u(t) \rangle$) is zero [19]. A statistical description of unrestricted diffusion as a Gaussian random process also shows that $\langle u(t_1)u(t_2) \rangle = 2D \zeta(t_2 - t_1)$, where D is the free (unrestricted) diffusion coefficient and ζ is the dirac delta function [19]. Since all cumulants other than second-order ($n = 2$) are zero for a Gaussian random process [23], substitution of previous results into Eq. (3) shows that [19]—

$$\lambda_u = -Db, \tag{11}$$

where the so-called gradient factor (b) is $\gamma^2 \int_0^\tau F^2(t') \, dt'$.

Eq. (11) describes the contribution axial diffusion makes to the cumulant expansion (λ_u) in Eq. (10). The other contribution (λ_V) arises from flow and is mediated by Brownian displacements across streamlines. To describe this it is useful to express ensemble averages over the random function $V(r(t))$ in terms of the stationary flow field V and the random position r for diffusing gas at different times—

$$\langle V(r(t_1))V(r(t_2)) \cdots V(r(t_n)) \rangle = \langle V(r_1)V(r_2) \cdots V(r_n) \rangle. \tag{12}$$

Here, r_1 is used as shorthand notation to represent the random position for a gas molecule at a time t_1 (i.e. $r(t_1)$) after its location is first encoded at r_0. Values for $r_2 \cdots r_n$ are similarly defined.

To evaluate the right side of Eq. (12) it is generally necessary to define the joint probability density (W_n) for different space-time trajectories that start from the encoded image location r_0 [25,30]. The ensemble average is then taken over all possible paths that originate from r_0 and pass through specified times.

Fig. 2 shows a trajectory that is described by $W_2(r_0|r_2, t_2; r_1, t_1)$ $dr_2 \, dr_1$. This utilizes time-ordered notation ($t_1 > t_2 > t_3 \cdots t_{n-1} > t_n$) and describes the probability for finding a gas molecule within a small, elementary volume dr_2 at (r_2, t_2), and then within dr_1 of (r_1, t_1)—after location is first encoded at r_0 [25]. As a stationary Markov process, each leg in the trajectory is statistically independent and probabilities only depend on time intervals between successive points [25,30]. In this case, the joint probability density function for trajectories of any order (W_n) can be defined conveniently using the diffusion propagator P, such that [25,30]—

$$W_n(r_0|r_n, t_n; r_{n-1}, t_{n-1} \cdots r_1, t_1) \\ = P(r_0|r_n, t_n)P(r_n|r_{n-1}, t_{n-1} - t_n) \cdots P(r_2|r_1, t_1 - t_2). \tag{13}$$

Generally, n propagators are used starting from the leftmost on the right side of the equality. Functionally, $P(r_0|r, t)dr$ describes the conditional probability that a gas molecule initially at r_0 will be within dr of r after a time t (19, 25, 30). Other propagators in Eq. (13) have the same functional form, but initial and final locations differ in order to describe all possible trajectories.

In practice, the above considerations provide a general theoretical framework for calculating ensemble averages over diffusing gas molecules in any stationary flow field (V). The general result for calculating the nth order ensemble average over any random function $V(r)$ has been used previously by others [24]—

$$\langle V(r(t_1))V(r(t_2)) \cdots V(r(t_n)) \rangle = \int_{r_1} dr_1 \int_{r_2} dr_2 \\ \cdots \int_{r_n} dr_n V(r_1)V(r_2) \cdots V(r_n)W_n(r_0|r_n, t_n; r_{n-1}, t_{n-1}; \cdots r_1, t_1). \tag{14}$$

2.4. 2D diffusion propagator for a cylindrical pipe

In a straight cylindrical pipe, diffusion over its cross-section determines how individual molecules sample the stationary flow
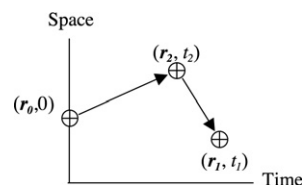

Fig. 2. Space-time trajectories for the second-order, joint probability density function (W_2).

field defined by Eq. (7). The propagator (P) is therefore governed by Fick's law, $D\nabla^2 P = \partial P/\partial t$, where D is the 'free' (i.e. unrestricted) molecular diffusion coefficient. This is conveniently solved in two-dimensions (2D) using cylindrical-polar coordinates (r, θ), and the initial condition that $P(r_0, \theta_0 | r, \theta, t = 0) = (1/r)\zeta(r - r_0)\ \zeta(\theta - \theta_0)$ where ζ is the Dirac delta function. To insure probability is conserved it is also required that $\partial/\partial t \int P(r_0, \theta_0 | r, \theta, t)r\,dr\,d\theta$ is always zero. Utilization of Fick's law and the divergence theorem then shows that a specific solution must satisfy $\partial P/\partial r = 0$ at all points on the pipe's surface. Under these conditions the diffusion propagator can be expressed in the following fashion [29]—

$$P(r_0, \theta_0 | r, \theta, t) = \sum_{j=0}^{\infty} \sum_{k=1}^{\infty} A_{jk}^2 e^{-\beta_{jk}^2 Dt/a^2} J_j(\beta_{jk} r/a) J_j(\beta_{jk} r_0/a) \cos(j(\theta - \theta_0)). \tag{15}$$

In this equation J_j denotes the jth order Bessel function, and β_{jk} is the kth root of—

$$d/dx(J_j(x)) = 0. \tag{16}$$

In addition, for $j \neq 0$

$$A_{jk}^2 = \left(\frac{2}{\pi a^2}\right) \frac{\beta_{jk}^2}{J_j^2(\beta_{jk})(\beta_{jk}^2 - j^2)}, \tag{17}$$

otherwise

$$A_{0k}^2 = \left(\frac{1}{\pi a^2}\right) \frac{1}{J_0^2(\beta_{0k})}. \tag{18}$$

A 2D analogy for Eq. (14) is then used to express the nth-order ensemble average of axial flow velocity in a straight pipe—

$$\langle V(\mathbf{r}(t_1))V(\mathbf{r}(t_2)) \cdots V(\mathbf{r}(t_n)) \rangle = \int_{r_1} \int_{\theta_1} r_1\,dr_1\,d\theta_1 \int_{r_2} \int_{\theta_2} r_2\,dr_2\,d\theta_2$$
$$\cdots \int_{r_n} \int_{\theta_n} r_n\,dr_n\,d\theta_n V(r_1)V(r_2)$$
$$\cdots V(r_n)W_n(r_0, \theta_0 | r_n, \theta_n, t_n; r_{n-1}, \theta_{n-1}, t_{n-1}, \ldots r_1, \theta_1, t_1). \tag{19}$$

Here, radial integrals vary from 0 to a, and integrals over θ are from 0 to 2π.

2.5. Defining apparent flow and diffusion

In most liquid-state applications molecular diffusion is not rapid enough to move excited nuclei across different flow streams during the imaging time. If intra-voxel dephasing is neglected, the relative phase for the spatially resolved MR signal at location $\mathbf{r}_0$ in a flow-encoded image ($\phi(\mathbf{r}_0)$) is just $\propto \bar{v}(\mathbf{r}_0)$, where $\alpha = \gamma \int_0^{\tau} F(t')\,dt'$, and $\bar{v}(\mathbf{r}_0)$ represents the average velocity over the resolved voxel. A plot of $\phi(\mathbf{r}_0)$ versus α at each location is therefore commonly employed for measuring regional fluid flow [16–19]. Here, the same approach is used to measure the *apparent* gas velocity (v_{app}) at each image location ($\mathbf{r}_0$). Predictions based on the numerical evaluation of the cumulant expansion (λ) are then formulated using the same definition, such that—

$$v_{app}(\mathbf{r}_0) = \frac{\phi(\mathbf{r}_0)}{\alpha} = \frac{\text{Im}\lambda}{\alpha}. \tag{20}$$

Similar rationale is used for defining the apparent gas diffusion coefficient—

$$D_{app}(\mathbf{r}_0) = \frac{\beta(\mathbf{r}_0)}{b} = -\frac{\text{Re}\lambda}{b}. \tag{21}$$

Particularly, since Eq. (11) shows that this yields a value for the gas diffusion coefficient (D) in the absence of flow.

3. Materials and methods

3.1. ^{3}He gas generation, delivery, and characterization for pipe flow

Recent work describes our apparatus for generating hyperpolarized (HP) ^{3}He [31]. Immediately before MR experiments, 0.4–0.5 L of ^{3}He gas with $\sim$40% polarization was released into a 2-L Tedlar bag (Jensen Inert Products, Coral Springs, FL) that resided inside an acrylic box located within the fringe field of the imaging magnet. During flow experiments, the box was pressurized to push HP gas out of the bag at a constant rate. Immediately after leaving, ^{3}He gas was diluted to $\sim$10-volume-percent by mixing it with another flow stream consisting of either N_2 or C_3F_8 gas. The resulting mixture then traveled into a Tygon hose that was $\sim$1 m long, had an inner diameter of 3.2 mm, and carried gas straight through the magnet bore. Generally, use of different binary gas mixtures provided a convenient way of altering the rate of ^{3}He diffusion so impact on acquired images could be examined.

During gas delivery the volumetric flow through the Tygon tube was measured to be $\sim$240 cc/min. This was monitored at the tube's outlet by bubbling each binary gas mixture into a (inverted) graduated cylinder filled with water. Measurements with and without ^{3}He then allowed determination of delivered gas fractions, and facilitated fine adjustment to achieve described conditions.

At $\sim$240 cc/min the average axial flow velocity in the Tygon tube ($\bar{v} = V_{max}/2$) was $\sim$0.5 m/s. At standard temperature and pressure (STP), the kinematic viscosity (v_k) of nitrogen is 1.4×10^{-4} m^2/s, and $v_k = 1.5 \times 10^{-5}$ m^2/s for C_3F_8 [32]. The Reynold's number (Re $= 2a\bar{v}/v_k$) for dilute mixtures with ^{3}He is therefore about 10 and 100, respectively. Since this is much lower than the transitional value to turbulance ($\sim$2100), flow under the specified conditions is expected to exhibit the radial velocity profile defined by Eq. (7).

Prior to imaging gas transport, a non-imaging gradient-echo experiment was employed to measure the diffusion coefficient for diluted ^{3}He in N_2 and C_3F_8 mixtures. To avoid flow-enhanced effects, motion-sensitizing gradients were applied transverse to the flow axis using a bipolar pulse pair [17] similar to that depicted in Fig. 1. The gradient pulse width (δ) was 0.5 ms and the leading-edge pulse-separation (Δ) was 0.6 ms. The measured ^{3}He diffusion coefficient transverse to flow in a 10-volume-percent mix with N_2 was 0.78 ± 0.04 cm^2/s. For the same fraction of ^{3}He in C_3F_8 the measured value was 0.36 ± 0.02 cm^2/s. Since the diffusion time ($\Delta - \delta/3$) was only $\sim$0.4 m, the root-mean-square displacement ($\sqrt{2Dt}$) for diffusing ^{3}He gas was $\sim$250 and 170 μm for mixtures with N_2 and C_3F_8, respectively. Given that both were much smaller than the tube diameter (3.2 mm), potential effects stemming from restricted diffusion on the measurement time-scale were negligible. This was confirmed later using the Chapman–Enskog theory of binary gas diffusion—which predicts similar ^{3}He diffusion coefficients [33].

3.2. 2D CTI of axial gas transport in a straight pipe

Visualization of ^{3}He axial gas transport was achieved using the 2D, CTI experiment depicted in Fig. 1. Imaging was performed at 2.0 T using a UNITYPlus console (Varian, Palo Alto, CA), a home-built 7-cm diameter radio-frequency volume coil, and a 30-cm diameter horizontal-bore magnet (Oxford Instruments, Oxford, UK) equipped with actively shield gradients characterized by 60 μs rise-times (Resonance Research Inc., Billerica, MA). During gas delivery, constant-time images were collected using a 1.0 cm × 1.0 cm field-of-view (FOV), and a 6.0-mm thick slice that was transverse to the central axis of the Tygon tube. The imaging pulse sequence utilized a 20 ms repetition time (TR), a receiver bandwidth of 1 kHz, and 64 phase-encoding steps along each pla-

nar direction. In all cases, the bipolar gradient was characterized by a pulse-duration (δ) of 300 μs, and two images were acquired—one with no motion-sensitizing gradient and the other with a finite amplitude (G).

To examine the effects of encoding duration, imaging was repeated using two different leading-edge pulse-separations (Δ). For $\Delta = 1$ ms, the gradient amplitudes were 0 and 4 G/cm; and for $\Delta = 4$ ms, they were 0 and 1 G/cm. Generally, this insured flow sensitivity (α) was the same. For each Δ-value, images were acquired in an interleaved fashion such that each point in k-space was sampled sequentially using both motion-sensitizing gradient amplitudes. The phase encode gradient was then incremented after 2 averages. Because two interleaved images were acquired, relative image attenuation was directly attributed to gas transport and was uninfluenced by either T_1- (signal loss inside the Tedlar bag) or T_2-relaxation.

After raw data collection, images were reconstructed on a 128×128 matrix using a phase-sensitive, 2D Fourier Transform. Analysis of images acquired without motion sensitizing gradients showed that the average signal-to-noise ratio (SNR) over the pipe was $\sim$100. Apparent flow velocity (Eq. (20)) was determined at each matrix location with an SNR $\geqslant 50$ by measuring the phase difference between data acquired with and without motion sensitizing gradients. Apparent diffusion (Eq. (21)) was determined by measuring relative attenuation. In both cases, gradient rise-time was ignored and motion-sensitizing gradient pulses in Fig. 1 were assumed to be square in shape. In this case, $\alpha = \gamma G \Delta \delta$ [17,18], $b = \gamma^2 G^2 \delta^2 (\Delta - \delta/3)$ [19], and it is noted that the gyromagnetic ratio (γ) for ^{3}He is 20,376 rad/(G s) [34]. Since apparent diffusion is determined by measuring relative attenuation, imaging gradients make no contribution to the b-value used in Eq. (21) [35]. Possible cross-terms with applied slice selection gradients are also zero because they refocus spins before motion-sensitizing gradients are applied [35].

3.3. Simulated pipe dynamics

Apparent transport in a straight pipe was predicted in *Mathematica* using Eqs. (20) and (21). Related code generally involved the numerical evaluation of the cumulant expansion (λ_V) and multi-dimensional integrals over the diffusion propagator defined in Eq. (15). The Appendix shows that significant simplification is possible because only the $j = 0$ terms contribute to angular integrals that define ensemble averages in Eq. (19), and that each of these is 2π.

To optimize the speed and accuracy of numerical calculations, apparent transport was evaluated multiple times using the first three terms in the cumulant expansion of Eq. (3) ($n = 3$). Generally, each evaluation was performed using either—(1) a different support (i.e. discrete sampling) for numerical integration, or (2) a different number of k-terms in the expansion for the diffusion propagator (Eq. (15)). The minimum values need for results to change less than a few percent after successive doublings were then chosen. This showed that only $\sim$32 k-terms were needed to achieve computational convergence comparable to the uncertainty of experimental data.

3.4. 2D airflow imaging in ventilated rats

Pulmonary airflow was visualized in Male Sprague–Dawley rats (Charles River Laboratories, Wilmington, MA) using 2D CTI and protocols approved by the Institutional Animal Care and Use Committee at Pacific Northwest National Laboratory. Prior to experiments, rats were anesthetized using 3–4% isoflurane in air. A tracheotomy was then performed and a 14-gauge catheter tube was inserted into the exposed trachea. After securing with surgical

string, each animal was placed in a supine position and its tracheal tube was attached to the mouthpiece of a home-built, computer-controlled, ventilator similar to described designs [36,37]. To facilitate animal positioning, the rat and mouthpiece were both secured on a wooden tray that also accommodated a NMR compatible ECG/temperature monitoring unit (SA Instruments Inc., Stony Brook, NY, Model 1025). The tray was then slid onto a mating rail that was located inside a double-tuned (^{1}H/^{3}He) RF coil [38].

During imaging, body temperature was maintained by circulated warm air inside the magnet bore. Body temperature and heart rate were monitoring using a rectal probe and ECG electrodes, respectively. To avoid possible RF interference, physiological data were fed via fiber optic to a dedicated laptop. Typically, rectal temperature was about 35 °C, and pulse rate was between 250 and 330 beats per minute.

Fig. 3 shows a typical respiratory maneuver used for imaging pulmonary airflow. During imaging, the maneuver was repeated every 1.6 s, and the pulse-sequence was applied during inhalation with a stationary flow rate. Delivered gas mixtures and drive pressures are specified in the caption. The trace in Fig. 3 shows the flow velocity through a calibrated pneumotach that was placed between the ventilator's mouthpiece and the attached rat [39]. It shows that gas speed is constant over the imaging window. Generally, in vivo CTI acquisition is similar to that used for visualizing pipe flow. In vivo imaging differs in that—(1) a thinner slice is employed to reduce volume averaging, (2) a lower flip angle is used to avoid saturation of inflowing magnetization, and (3) a shorter TR is employed to allow 32 acquisitions during the constant flow window. Specific values for each are therefore specified in later figures.

3.5. 3D imaging of rat pulmonary airway structure and flow

Extending MR imaging to 3D for visualizing pulmonary structure and flow in ventilated rats exploited two recent technical developments. First, more ^{3}He gas was generated by using larger oblong polarization cells and two parallel lasers. Two cells (each containing $\sim$0.8 L) could then be pumped simultaneously [31]. The second development was to employ a hybrid, radial imaging scheme for more efficient k-space sampling [31]. The 3D pulse-sequence employs a low flip-angle ($\sim$10°) excitation that is followed by bi-polar motion-sensitizing gradient like that shown in Fig. 1. Spatial location is then encoded using a 2D radial
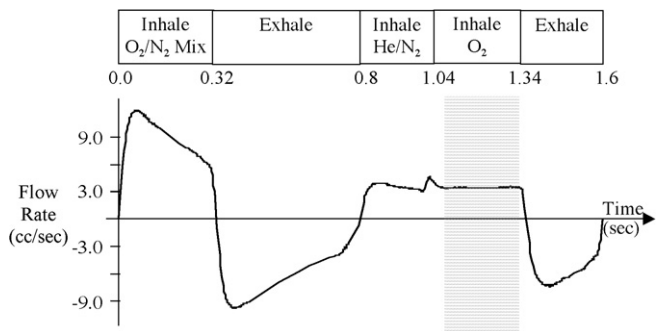

Fig. 3. Typical respiratory maneuver for in vivo airflow imaging. Boxes along top show gas delivery events and the trace depicts the rate of flowing gas (cc/s) when measured with a calibrated pneumotach. The O_2/N_2 is a 30:70 volume mix that is delivered using a drive pressure of $\sim$11 cm H_2O, and the He/N_2 is about a 70:30 volume mix (delivered at $\sim$10 cm H_2O). Imaging occurs in the shaded region during a push of oxygen (O_2). The O_2 is delivered using a drive pressure of about 33 cm H_2O, and constant flow is achieved by forcing gas through a commercial restrictor (Airtronics, Bellevue, WA, 0.012″ orifice diameter, model # F2815-121-B85). Generally, differences in drive pressure and flow reflect the unique delivery route and plumbing for each gas mixture and do not reflect actual pressure at the trachea.

sampling scheme in conjunction with standard phase encoding along the orthogonal direction [31].

Unlike in 2D imaging studies, rats used for 3D visualization were orally intubated. Prior to intubation, rats were administered 0.02 mL/kg BW glycopyrrolate subcutaneously to inhibit oral secretions and facilitate insertion of an endotracheal tube. After 10–15 min, the animals were then anesthetized with isoflurane and placed supine on a tilting intubation table. Approximately, 0.02 mL of lidocane was then applied directly to the larynx. Shortly thereafter, a 14 gauge catheter tube was orally inserted into the trachea. The tube was pre-cut to a length to assure that it would pass through the larynx but not come near the carina. Once inserted, the catheter tube was connected to the ventilator.

In the current study gas from two polarization cells was used for each rat. Gas from the first cell was used to acquire a high-resolution view of pulmonary airways. Raw data were collected using 128 phase encodes and 200 radial projections with 128 complex points. The FOV was 6.4 cm on a side and the acquisition bandwidth was 51 kHz. The hybrid pulse sequence utilized a 500 ms hard RF pulse together with an 8 ms TR and no motion encoding. The acquired signal consisted of an asymmetric gradient echo that refocused 1.085 ms after the center of the RF excitation. Image reconstruction was then done as before [31]. During the breathing maneuver shown in Fig. 3, 32 phase-encoded projections were acquired during inhalation with a stationary flow rate. The maneuver was then repeated 800 times for a total acquisition length of 21 min. To reduce possible blurring, the O_2 push was reduced by decreasing the drive pressure to ∼4 cm H_2O.

After gas in the first ^{3}He cell was used for high-resolution imaging, O_2 drive pressure was increased to the level specified in Fig. 3. Then, the second ^{3}He cell was utilized for lower-resolution, 3D flow visualization in the same animal. Raw data were collected using 4 interleaved, 3D acquisitions that employed 32-phase-encodes and 128 radial projections comprised of 128 complex points. One 3D acquisition utilized 4 G/cm for motion sensing along the magnet's x-axis, another used 4 G/cm along its y-axis, the third employed 3 G/cm along z, and finally, the fourth had none. With 32 acquisitions for every breathing maneuver, data collection required 512 repetitions for a total acquisition time of ∼14 min. All 3D images used the same TR (8 ms), had a refocus time of 2.385 ms for the collected echo, and employed the same timing for motion-sensitizing gradients ($\delta = 0.3/\Delta = 1.0$ ms).

4. Results and discussion

4.1. Simulated pipe flow and the Gaussian approximation

Eq. (19) shows that the average axial flow velocity for an ensemble of molecules originally at $\mathbf{r}_0$ inside a straight cylindrical pipe varies with time, such that—

$$\langle v(t) \rangle = \int_{r=0}^{a} \int_{\phi=0}^{2\pi} P(\mathbf{r}_0 | r, \phi, t) V(r) r \, dr \, d\phi. \quad (22)$$

Substituting with Eq. (15) and evaluating integrals then gives—

$$\langle v(t) \rangle = \frac{V_{\max}}{2} + 4\pi V_{\max} a^2 \sum_{k=2}^{\infty} \frac{A_{0k}^2}{\beta_{0k}^2} e^{-\beta_{0k}^2 D t / a^2} J_0(\beta_{0k} r_0 / a) J_2(\beta_{0k}). \quad (23)$$

The time-dependence embodied by Eq. (23) shows that the average axial flow velocity for ^{3}He gas originally encoded at r_0 (in a CTI image) approaches $V_{\max}/2$ at long times. At shorter times, the precise behavior depends on the initial radial position (r_0), the ^{3}He diffusion coefficient (D), and the time t after spatial encoding (see Fig. 1). This general behavior is illustrated in Fig. 4 where $\langle v(t) \rangle$ is plotted as a function of time for molecules starting at the center of the pipe (dashed) and its edge (solid). Projected behavior shows that gas

molecules near the edge accelerate to the average flow velocity ($V_{\max}/2.0$), whereas molecules at the center slow to the same value. Generally, the approach to average flow is more rapid at the edge because the radial derivative of $V(r)$ in Eq. (7) is steeper at that location. Consequently, as gas diffuses across different flow streams, molecules initially at the edge experience a larger change in velocity—that then drive's their more rapid approach to the average axial flow speed ($V_{\max}/2$).

In practice, the temporal dependence of $\langle v(t) \rangle$ has a significant impact on the apparent axial velocity (v_{app}) calculated using Eq. (20). Mathematically, this is because $\langle v(t) \rangle$ defines the first-order ($n = 1$) term in the cumulant expansion of Eq. (3). Since this is imaginary it defines the lowest order contribution to apparent velocity. After integration (over $F(t)$) the result is used in Eq. (20) to formulate a first-order approximation to the apparent velocity ($^1v_{app}$). Since Eq. (20) shows that only imaginary terms contribute to v_{app}, and Eq. (3) shows these are all odd, the next highest order contribution comes from the third term in the cumulant expansion ($^3v_{app}$), such that $v_{app} = {}^1v_{app} + {}^3v_{app} + \cdots$

A plot of $^1v_{app}$ is shown in Fig. 5 as a function of radial location in a 3.2-mm diameter straight pipe. Predicted results are formulated using $t = 0.425$ ms as the start of motion encoding, $G = 4$ G/cm, $\Delta = 1.0$ ms, $\delta = 0.3$ ms, and the same conditions specified in Fig. 4. The axial velocity profile predicted by Eq. (7) is also shown in Fig. 5 for comparison. Differences illustrate how rapid gas diffusion blurs the apparent axial flow so it no longer resembles predictions based solely on the Navier–Stokes equation. By comparison, apparent axial flow is seen to be significantly slower than Eq. (7) predicts at the center of the pipe, and is faster at the pipe edge—as expected from the behavior of $\langle v(t) \rangle$ seen in Fig. 4.

Fig. 5 also shows a plot for the third-order contribution to the apparent flow velocity ($^3v_{app}$). This is seen to be comparatively small and provides valuable insight into the relative influence of higher order terms in the cumulant expansion. From a practical standpoint, this is important for determining how many terms in Eq. (3) are necessary for making accurate predictions. If too few
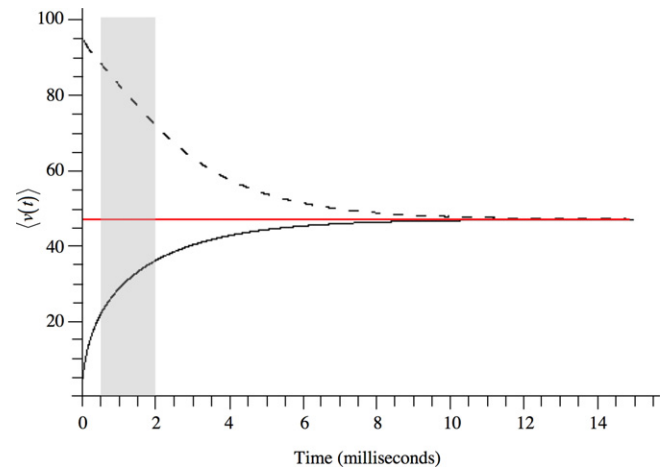

Fig. 4. Predicted average axial flow velocity $\langle v(t) \rangle$ in cm/s for dilute ^{3}He gas after location in a straight tube is initially encoded at $t = 0$ using the CTI pulse sequence shown in Fig. 1. Flow dynamics were calculated for a 10% volume mixture of ^{3}He in N_2 using Eq. (23), a tube radius (a) of 0.16 cm, a maximum flow velocity ($V_{\max}$) of 94.4 cm/s, and 0.78 cm²/s for the ^{3}He diffusion coefficient (D) in the binary gas mixture. The red line shows the average flow velocity ($V_{\max}/2 = 47.2$ cm/s) across the pipe, and this corresponds to a volume flow rate of approximately 228 cc/min. The dashed line shows the average axial velocity predicted for gas molecules starting from the middle of the tube ($r = 0$), and the solid line shows the average velocity for gas initially encoded at the tube's edge ($r = a$). The shaded region highlights the sampling area of motion sensitizing gradients (i.e. non-zero $F(t)$) for conditions specified in Fig. 5.
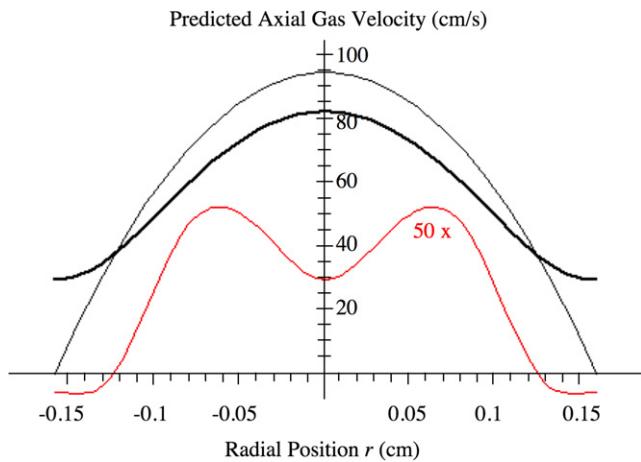
Fig. 5. Predicted axial velocity for gas in a straight tube when bi-polar, motion-sensitizing gradients in Fig. 1 start at $t = 0.425$ ms, $G = 4$ G/cm, $\Delta = 1.0$ ms, and $\delta = 0.3$ ms. Gas properties, tube radius, and flow conditions are specified in Fig. 4. Predictions based on the solution to the Navier–Stokes equations ($V(r)$ in Eq. (7)) are plotted in black, the first-order ($n = 1$) approximation to apparent flow velocity ($^1v_{app}$) in Eq. (20) is shown in bold, and 50 times the third-order ($n = 3$) contribution to apparent flow ($^3v_{app}$) is shown in red.

are used achieved accuracy will likely be insufficient, and if too many are employed unnecessary computations will be performed. In prior work, contributions from higher order terms were considered when the correlation time for molecular motion is much shorter than the imaging time [20,21]. In this study, Fig. 4 shows that motion is more slowly varying. Consequently, the relative importance of higher order approximations needs reconsideration.

At the onset of this study the relative importance of higher order contributions to the cumulant expansion would be difficult to predict. A general formulation of motion effects is therefore formulated. The benefit of this is that simplifying assumptions about relative contributions can now be made and tested directly using $^1v_{app}$ and $^3v_{app}$ in Fig. 5.

During the pulse-sequence shown in Fig. 1, $F(t)$ (from Eq. (2)) quickly reaches a minimum value of $F = -\gamma G\delta$. It then remains at that value for a time Δ, after which, it returns to zero. Over the time Δ, when velocity is effectively sampled, gas molecules initially encoded at each location $\boldsymbol{r}_0$ will exhibit some average value that can be determined directly from $\langle v(t) \rangle$ in Fig. 4. Since the higher order cumulants describe the statistical deviation dv from this average, contributions in Eq. (3) can be expressed in powers of Fdv [20]. If dv is slowly varying over Δ, the nth term in Eq. (3) is then of the order $(1/n!)(dv\Delta F)^n$ when $n > 1$. To validate this scaling relationship, consider the shaded region in Fig. 4. There, it is seen that the flow velocity for diffusing gas at different locations changes by an amount (dv) that is ~20 cm/s when $F(t)$ is non-zero. Since $\Delta = 0.001$ s and $F = -\gamma G\delta = 24.5$ radian per cm, the third-order ($n = 3$) contribution to Eq. (3) is estimated (i.e. $(1/3!)(dv \Delta F)^3$) to be ~0.019 radian. Given $\alpha = \gamma G\Delta\delta$ in Eq. (20), and this is 0.024 radian · s/cm under the specified conditions, $n = 3$ contributions to the apparent axial velocity ($^3v_{app}$) in Eq. (20) are then predicted to be ~0.8 cm/s. Comparison with the actual third-order term in Fig. 5 shows that this is very nearly what is calculated; thereby, validating proposed scaling.

Fig. 5 shows that third-order contributions to apparent flow are only about 2% of the first-order term. Because this is smaller than experimental uncertainty, higher order contributions are safely neglected. Importantly, the same scaling arguments hold for estimating relative contributions to the apparent diffusion coefficient (D_{app}) defined through Eq. (21). In this case $(1/n!)(dv \Delta F)^n$ is about 0.12 for $n = 2$ and ~0.002 for $n = 4$. Approximating D_{app} by only the

second-order ($n = 2$) term in the cumulant expansion is therefore again accurate to about 2%.

The above considerations justify approximation of the cumulant expansion using the first and second terms for calculating apparent flow and diffusion, respectively. In practice, this is termed a Gaussian approximation because all cumulants higher than second-order are exactly zero for a Gaussian random process [23]. Since this can be achieved experimentally simply by adjusting Δ and/or F, its importance to apparent transport studies cannot be over emphasized [20,21].

4.2. Apparent ^3He gas transport and size effects in a straight pipe

Apparent ^{3}He velocity measurements in a straight pipe are summarized in Fig. 6. Generally, excellent agreement is found between experimental data and predictions based on a first-order ($n = 1$) approximation to Eq. (20). Images acquired using different Δ values illustrate how blurring of laminar flow structure becomes more severe as time is lengthened to apply motion-sensitizing gradients. Nevertheless, flow rates (cc/s) determined by integrating the apparent velocity (v_{app}) over the pipe cross-section remain constant and are generally within ~10% of experimental values. Measurements of apparent ^{3}He velocity therefore provide a quantitative basis for measuring regional flow rates—even when flow structure is blurred in small conduits. This is predicted mathematically simply by integrating the first-order approximation to Eq. (20) over the pipe's cross-section and noting the diffusion propagator is normalized. The result is that flow rates measured from imaging data are always equal to the value predicted from the Navier–Stokes solution in Eq. (7).

Laminar flow structure in Fig. 6 shows that the degree of blurring depends on the binary gas mixture—being more pronounced when ^{3}He is diluted in N_2 rather than with C_3F_8. Physically, this is expected since ^{3}He diffusion in N_2 (~0.78 cm^2/s) is about twice as fast as for ^{3}He in C_3F_8 (~0.36 cm^2/s). Since the diffusion coefficient for HP ^{129}Xe is ~10 times lower (1), it is potentially useful if the goal is to visualize more laminar flow structure in small conduits. Its lower sensitivity relative to ^{3}He, however, would inevitably reduce achievable resolution so some compromises would be required.

Measured and predicted values for apparent axial ^{3}He diffusion are summarized in Fig. 7. Like with apparent flow, close agreement is observed between experimental data and formulated predictions. Images acquired using different Δ values illus-
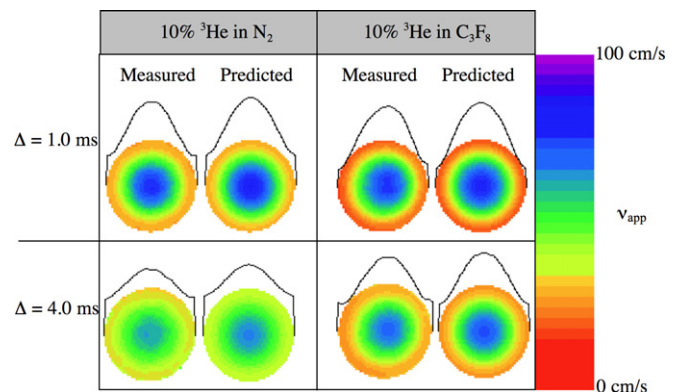

Fig. 6. Apparent axial ^{3}He gas flow in a straight, 3.2-mm diameter tube. Predictions for apparent flow (v_{app}) are based on the first-order ($n = 1$) approximation and are formulated using a V_{max} value derived from measured volume flow. In each image, the black plot shows the radial profile for axial flow across the tube diameter. Average uncertainty in measured velocity for all 4 experiments is estimated to be ±1.3 cm/s using the known α-values and the measured signal-to-noise ratio in acquired images [40].

trate how axial diffusion is enhanced as more time is allowed for molecules to traverse multiple streamlines. Not surprisingly, the precise enhancement is seen to vary with gas mixture. Less expected is that the apparent diffusion exhibits a laminar-like structure that reaches a maximum about midway between the pipe's center and wall. Generally, this reflects complex gas dynamics and the behavior of the second-order cumulant in Eq. (5).

Predicted images of apparent flow velocity in pipes of different size are shown in Fig. 8. These simulated results suggest that laminar structure should be clearly observed in larger pipes with sizes comparable to those in human pulmonary airways. Significant blurring of laminar flow is, however, expected in smaller airways—like those in the major airways of rodents.

4.3. 2D and 3D pulmonary airflow imaging in ventilated rats

Fig. 9 shows measured ^{3}He gas flow in 2D constant-time images of rat pulmonary airways. Because a tracheotomy was employed,

Fig. 7. Apparent axial ^{3}He gas diffusion during laminar flow in a straight, 3.2-mm diameter tube. Flow conditions are the same as in Fig. 6, and predictions (for D_{app}) are based on a second-order ($n = 2$) approximation. In each image, the black plot shows the radial profile for axial diffusion across the tube diameter. Uncertainty in measured diffusion is estimated from known b-values and the measured signal-to-noise ratio in acquired images [41]. For $\Delta = 1.0$ ms uncertainty is estimated to be ±0.03 cm^2/s, and for $\Delta = 4.0$ ms it is ±0.15 cm^2/s. All plots include a contribution of D that represents the free gas diffusion coefficient in the absence of flow. For ^{3}He in N$_2$ $D = 0.78 \pm 0.04$ cm^2/s, and for ^{3}He in C$_3$F$_8$ $D = 0.36 \pm 0.02$ cm^2/s.

Fig. 8. Predicted apparent axial ^{3}He gas flow in tubes of different diameter (2a). Predictions are based on a first-order ($n = 1$) approximation ($^1v_{app}$) using the gradient parameters specified in Fig. 5. *Top row from left to right:* Navier–Stokes prediction for a straight pipe of any radius, $^1v_{app}$ for $a = 11$ mm, and $a = 6$ mm. *Bottom row:* $^1v_{app}$ for $a = 3$, $a = 1.5$, and $a = 0.5$ mm. In each image, the black plot shows the radial profile for axial flow across the tube diameter.

inhaled gas flowed straight into the rat trachea. Consequently, measured flow in the trachea was similar to that seen in a straight pipe of comparable size. Similarities illustrated in Fig. 9B include a non-zero axial velocity at the edge of the trachea, and a blurred laminar flow profile.

Although some flow structure is evident in the rat trachea, Fig. 9C shows that nothing comparable is observed at the lung's first bifurcation. Analysis of 3D flow data suggests that this is mainly due to not measuring all the vector flow components. Before this is examined, however, the more obvious is first noted. Namely, that flow at the bifurcation is significantly slower than in the trachea. Physically, this is because mass conservation requires flow to slow when it splits to fill the right and left bronchi. During inhalation, this is expected to occur at every successive bifurcation—as gas moves deeper down the airway tree. A high degree of correlation is therefore anticipated between measured gas speed and airway branching structure.

Fig. 10A shows a maximum intensity projection of 3D rat pulmonary airways observed using radial-hybrid ^{3}He imaging. Results provide a detailed view of branching topology that feeds inhaled air to each of the rat's five lung lobes [42]. More remarkable, however, is that all major airways are distinguished in Fig. 10B, where effects on the calculated velocity magnitude resulting from the combination of measured components are shown in full 3D. Flow data were acquired in the same rat; thereby, providing detailed information about both airway structure and inhaled gas dynamics.

Besides flow splitting, gas streaming is also observed in 3D data. Generally, streaming is characterized by a narrow region of faster flow along the airway's outside radius of curvature. In humans, this has been visualized in 2D images of ^{3}He flow through the trachea [2]. Fig. 10C shows similar transport in the rat trachea. Presumably,
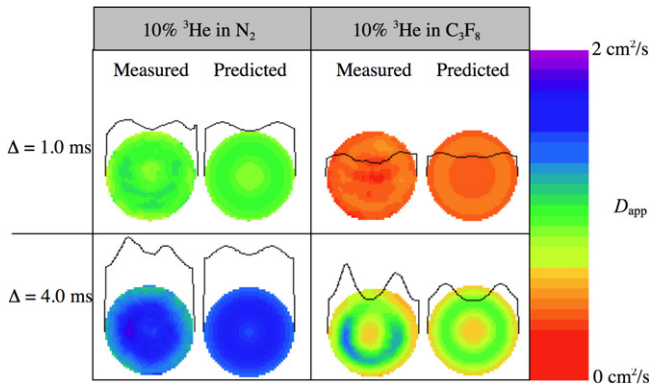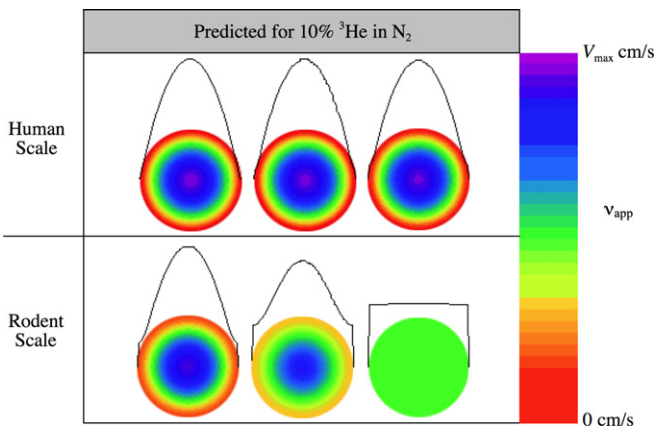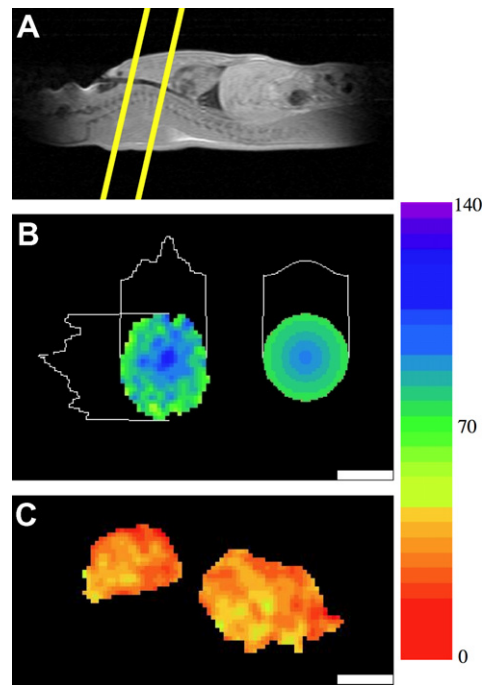

Fig. 9. 2D CTI of pulmonary airflow in a 220 g rat. (A) Sagittal proton image showing slice locations for ^{3}He flow visualization. (B) *Left:* measured flow speed normal to the slice plane in the rat trachea. (B) *Right:* simulated apparent velocity in a straight pipe of comparable size and volume flow (~2 cc/s). White traces show flow profiles across the center and the bold scale bar represents 1 mm. (C) Flow speed normal to the slice plane in the bronchi. All images were acquired using a 3 mm thick slice, a 10° flip angle, a square FOV 1.0 cm on a side, and an 8 ms TR. The color scale shows measured flow speed (cm/s) and uncertainty is estimated to be ±10 cm/s using established methods [40].
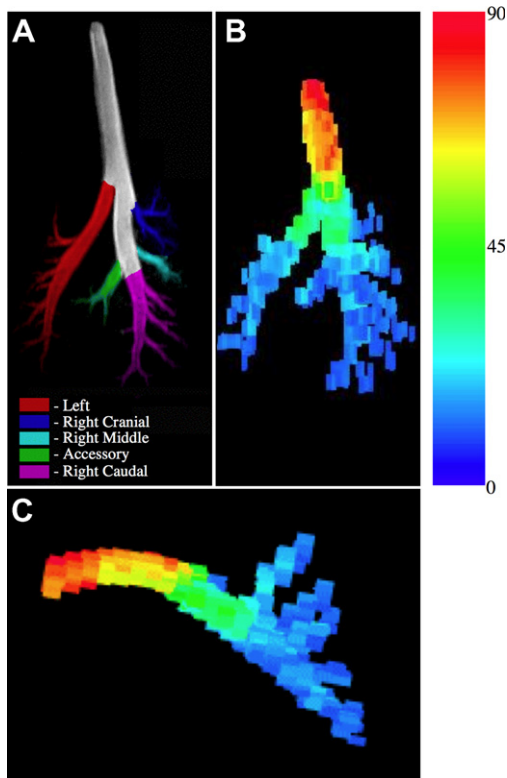
Fig. 10. 3D imaging of pulmonary structure and flow in a 322 g rat. (A) Maximum intensity projection of 3D airway structure visualized with high-resolution, hybrid, radial imaging. Colorized airways highlight main branches feeding the rat lung's five lobes. Raw image data is zero-filled once along each dimension. (B) 3D rendering of velocity magnitude calculated from lower resolution, motion-sensitized, radial-hybrid images. The color scale shows calculated velocity magnitude (cm/s) and uncertainty is estimated to be ±2 cm/s using established methods [40]. Flow results are not rendered using the same software employed for (A), and as a consequence, viewing angles are not strictly the same. No zero-fill is employed prior to reconstructing flow images. It is also noted that flow is not analyzed higher up in the trachea because signal drops off more severely due to the dilution of ^{3}He from the extra O_2 push used for flow measurements (see Section 3.4). (C) 3D flow viewed from the same perspective as the sagittal image shown in Fig. 9A.

this was not observed in initial 2D experiments because use of a tracheotomy insured that gas flowed straight into the lung. With oral intubation and the rat in a supine position, gas must travel along a more curved path—as illustrated in Fig. 10C. Slice-by-slice inspection of 3D flow data shows that streaming in the trachea continues down the entire branching structure along the same outside edge. It was also found that streaming was most evident when all the vector components are acquired. Conceptually, this is not surprising since airflow in deeper branches is generally oblique relative to the laboratory frame in which motion-sensitizing gradients are applied. In this context, 3D vector mapping is critical to completely capture actual gas dynamics.

The measured flow speed shown in Fig. 10B and C is a scalar representation of the full vector flow field. Generally, this provides a quantitative view of pulmonary gas delivery not previously seen. Although measured velocity is inevitably blurred, significant slowing due to major airway branching is still observed. Like in straight pipes, it is also expected that measured flow rates in each branch are quantitative. To illustrate this, gas flow (cc/s) was measured in each of the five colored airways shown in Fig. 10A. Flow was determined in two steps. First, data in Fig. 10A was used for measuring the cross sectional area for each airway feeding a different lung lobe. Gas flow was then calculated using the vector dot product between the measured area, a unit vector normal to the airway's cross section, and the aver-

age gas velocity vector that is measured at the same location from lower resolution data used for generating Fig. 10B–C. The results are 0.86 ± 0.04, 0.70 ± 0.07, 0.18 ± 0.01, 0.22 ± 0.03, and 0.21 ± 0.03 cc/s for flow in the left, right caudal, right middle, right cranial, and accessory lobes, respectively. The total flow determined from imaging data is therefore 2.17 ± 0.18 cc/s. Prior to imaging, the actual flow rate was measured to be 2.31 ± 0.02 cc/s using a calibrated pneumotach. Total flow measured with MRI is therefore in good agreement (within 6%) with known ventilation settings. Results might therefore provide a quantitative basis for measuring lobar ventilation in pre-clinical animal models. If possible, it may then become feasible to monitor changes with disease, and to relate these to alterations in down stream lung compliance.

Observation of gas streaming in the rat airways generally highlights that some laminar flow structure is discernable. In animal models, this could be useful for understanding the deposition of inhaled materials. In the past, CFD modeling has been used to begin understanding related issues. A full CFD model of the rat respiratory system has, however, never been developed or tested. The work described here represents an integral part of our ongoing efforts to exploit MR imaging for developing and validating CFD models for the rat respiratory tract [6]. Current work is aimed at exploiting the analytical techniques described here to predict apparent ^{3}He flow from CFD predictions; thereby, providing a basis for future comparisons in live animals.

5. Conclusions

An analytical description of apparent gas transport accurately predicts measured ^{3}He gas dynamics in straight pipes, and shows that diffusion-mediated effects blur laminar flow structure in rodent-sized airways. Nevertheless, 3D airflow imaging in rodents reveals a detailed picture of lobar airflow not previously seen. This includes flow splitting from airway branching as well as flow streaming along the outside radius of curvature.

Acknowledgments

Appendix

Angular contributions to Eq. (20) are generally of the following form—

$$\int_{\theta_1=0}^{2\pi} d\theta_1 \int_{\theta_2=0}^{2\pi} d\theta_2 \cdots \int_{\theta_n=0}^{2\pi} d\theta_n \; \cos(j(\theta_1 - \theta_2)) \qquad (A.1)$$
$$\cos(j'(\theta_2 - \theta_3)) \cdots \cos(j''(\theta_n - \theta_0)),$$

where $j, j',$ and j'' represent summation indices from expansions like that defined in Eq. (15). Simplification is achieved by first noting—

$$\cos(j(\theta_1 - \theta_2)) = \cos(j\theta_1)\cos(j\theta_2) + Sin(j\theta_1)Sin(j\theta_2). \qquad (A.2)$$

Integration of Eq. (A.2) over θ_1 then gives 2π for $j = 0$ and is zero otherwise. The series therefore reduces to—

$$2\pi \int_{\theta_2=0}^{2\pi} d\theta_2 \cdots \int_{\theta_n=0}^{2\pi} d\theta_n \cos(j'(\theta_2 - \theta_3)) \cdots \cos(j''(\theta_n - \theta_0)). \qquad (A.3)$$

Expanding $\cos(j'(\theta_2 - \theta_3))$ like in Eq. (A.2) and integrating over θ_2 is then again 2π for $j' = 0$ and zero otherwise. Repeating the procedure for each successive cos term in (A.1) therefore collapses the entire series to give $(2\pi)^n$ if all j's are 0. For other j-values the integral series is zero.

References

[1] L.G. Kaiser, J.W. Logan, T. Meersmann, A. Pines, Dynamic NMR microscopy of gas phase Poiseuille flow, J. Magn. Reson. 149 (2001) 144–148.

[2] L. de Rochefort, X. Maitre, R. Fodil, L. Vial, B. Louis, D. Isabey, C. Croce, L. Darrasse, G. Apiou, G. Caillibotte, J. Bittoun, E. Durrand, Phase-contrast Velocimetry With Hyperpolarized ^{3}He for In Vitro and In Vivo Characterization of Airflow, Magn. Reson. Med. 55 (2006) 1318–1325.

[3] E. Brunner, M. Haake, L. Kaiser, A. Pines, J.A. Reimer, Gas flow MRI using circulating laser-polarized ^{129}Xe, J. Magn. Reson. 138 (1999) 155–159.

[4] R.W. Mair, M.S. Rosen, R. Wang, D.G. Cory, R.L. Walsworth, Diffusion NMR methods applied to xenon gas for materials study, Magn. Reson. Chem. 40 (2002) S29–S39.

[5] L. de Rochefort, L. Vial, R. Fodil, X. Maitre, B. Louis, D. Isabey, G. Caillibotte, M. Thiriet, J. Bittoun, E. Durand, G. Sbirlea-Apiou, In vitro validation of computational fluid dynamics simulation in human proximal airways with hyperpolarized ^{3}He magnetic resonance phase-contrast velocimetry, J. Appl. Physiol. 102 (2007) 2012–2023.

[6] K.R. Minard, D.R. Einstein, R.E. Jacob, S. Kabilan, A. Kuprat, C. Timchalk, L. Trease, R.A. Corley, Application of magnetic resonance (MR) imaging for the development and validation of computational fluid dynamic (CFD) models of the rat respiratory system, Inhalation Toxicol. 18 (2006) 787–794.

[7] I.V. Koptyug, S.A. Altobelli, E. Fukushima, A.V. Matveev, R.Z. Sagdeev, Thermally polarized ^{1}H NMR microimaging studies of liquid and gas flow in monolithic catalysts, J. Magn. Reson. 147 (2000) 36–42.

[8] B. Newling, C.C. Poirier, Y. Zhi, J.A. Rioux, A.J. Coristine, D. Roach, B.J. Balcom, Velocity imaging of highly turbulent gas flow, Phys. Rev. Lett. 93 (15) (2004) 154503-1–154503-4.

[9] M. Brandl, A. Haase, Molecular diffusion in NMR microscopy, J. Magn. Reson. 103 B (1994) 162–167.

[10] P.T. Callaghan, C.D. Eccles, Diffusion-limited resolution in nuclear magnetic resonance microscopy, J. Magn. Reson. 78 (1988) 1–8.

[11] C.B. Ahn, Z.H. Cho, A generalized formulation of diffusion effects in micron resolution nuclear magnetic resonance imaging, Med. Phys. 16 (1) (1989) 22–28.

[12] S. Gravina, D.G. Cory, Sensitivity and resolution of constant-time imaging, J. Magn. Reson. 104 (Series B) (1994) 53–61.

[13] S. Choi, X-W Tang, D.G. Cory, Constant time imaging approaches to NMR microscopy, Int. J. Imaging Syst. Techn. 8 (1997) 263–276.

[14] P.J. Prado, B.J. Balcom, I.V. Mastikhin, A.R. Cross, R.L. Armstrong, A. Logan, Magnetic resonance imaging of gases: a single-point ramped imaging with T1 enhancement (SPRITE) study, J. Magn. Reson. 137 (1999) 324–332.

[15] K.R. Minard, C. Timchalk, R.A. Corley, T_2-shortening of ^{3}He gas by magnetic microspheres, J. Magn. Reson. 173 (2005) 90–96.

[16] J. Stepisnik, Measuring and imaging of flow by NMR, Prog. NMR Spectrosc. 17 (1985) 187–209.

[17] A. Caprihan, E. Fukushima, Flow measurements by NMR, Phys. Rep. 198 (4) (1990) 195–235.

[18] J.M. Pope, S. Yao, Quantitative NMR of imaging of flow, Concepts Magn. Reson. 5 (1993) 302–381.

[19] P.T. Callaghan, Principles of Nuclear Magnetic Resonance Microscopy, Oxford University Press Inc., New York, 1993.

[20] J. Stepisnik, Validity limits of Gaussian approximation in cumulant expansion for diffusion attenuation of spin echo, Physica B 270 (1999) 110–117.

[21] A.F. Frøhlich, L. Østergaard, V.G. Kiselev, Effect of impermeable boundaries on diffusion-attenuated MR signal, J. Magn. Reson. 179 (2006) 223–233.

[22] R. Kubo, Generalized cumulant expansion method, J. Phys. Soc. Jpn. 17 (1962) 1100–1120.

[23] R. Kubo, A stochastic theory of line-shape and relaxation, in: D. ter Haar (Ed.), Fluctuation, Relaxation, and Resonance in Magnetic Systems, Oliver and Boyd, London, 1962, pp. 23–68.

[24] J.H. Freed, Generalized cumulant expansions and spin-relaxation theory, J. Chem. Phys. 49 (1968) 376–391.

[25] J.A. McLennan, Introduction to Non-Equilibrium Statistical Mechanics, Prentice Hall, New Jersey, 1989.

[26] D.O. Kuethe, Measuring distributions of diffusivity in turbulent fluids with magnetic resonance imaging, Phys. Rev. A 40 (8) (1989) 4542–4552.

[27] L.D. Landau, E.M. Lifshitz, Fluid Mechanics, Pergamon Press, London, 1959.

[28] R.B. Bird, W.E. Stewart, E.N. Lightfoot, Transport Phenomena, 2nd ed., John Wiley & Sons Inc., New York, 2002.

[29] A.L. Sukstanskii, D.A. Yablonskiy, Effects of restricted diffusion on MR signal formation, J. Magn. Reson. 157 (2002) 92–105.

[30] M.C. Weng, G.E. Uhlenbeck, On the theory of the Brownian motion II, Rev. Mod. Phys. 17 (1945) 323–342.

[31] R.E. Jacob, G. Laicher, K.R. Minard, 3D MRI of non-Gaussian 3He gas diffusion in the rat lung, J. Magn. Reson. 188 (2) (2007) 357–366.

[32] http://encyclopedia.airliquide.com/encyclopedia.asp.

[33] X.J. Chen, H.E. Moller, M.S. Chawla, G.P. Cofer, B. Driehuys, L.W. Hedlund, G.A. Johnson, Spatially resolved measurements of hyperpolarized gas properties in the lung in vivo. Part I: diffusion coefficient, Magn. Reson. Med. 42 (1999) 721–728.

[34] R.C. Weast (Ed.), CRC Handbook of Chemistry and Physics, CRC Press, Cleveland, OH, 1974.

[35] P.B. Kingsley, Introduction to diffusion tensor imaging mathematics: part II. Anisotropy, diffusion-weighting factors, and gradient encoding schemes, Concepts Magn. Reson. A 28 (2006) 123–154.

[36] L.W. Hedlund, G.P. Cofer, S.J. Owen, G.A. Johnson, MR-compatible ventilator for small animals: computer-controlled ventilation for proton and noble gas imaging, Magn. Reson. Imaging 18 (2000) 753–759.

[37] J.P. Dugas, J.R. Garbow, D.K. Kobayashi, M.S. Conradi, Hyperpolarized He-3 MRI of mouse lung, Magn. Reson. Med. 52 (2004) 1310–1317.

[38] T. Lanz, J. Ruff, A. Weisser, A. Haase, Double tuned Na-23 H-1 nuclear magnetic resonance birdcage for application on mice in vivo, Rev. Sci. Instrum. 72 (2001) 2508–2510.

[39] K.R. Minard, R.A. Wind, R.L. Phelps, A compact respiratory-triggering device for routine microimaging of laboratory mice, JMRI 8 (1998) 1343–1348.

[40] A. H Anderson, J.E. Kirsch, Analysis of noise in phase contrast MR imaging, Med. Phys. 23 (1996) 857–869.

[41] R.L. O'Halloran, J.H. Holmes, T.A. Altes, M. Salerno, S.B. Fain, The effects of SNR on ADC measurements in diffusion-weighted hyperpolarized He-3 MRI, J. Magn. Reson. 185 (2007) 42–49.

[42] P. Popesko, V. Rajtova, J. Horak, Anatomy of Small Laboratory Animals. Volume Two: Rat, Mouse, Hamster, Wolfe Publishing, London, 1992.